*minerals*

MDPI

*Article*

# Density Functional Theory Study on Structure and Properties of Sulfurized Cerussite (110) Surface

**Cong Han [1,2,*], Yuxin Ao [1,*], Yanbai Shen [1], Sikai Zhao [1], Qiang Zhao [1] and Shijie Zhou [1]**

[1] School of Resources and Civil Engineering, Northeastern University, Shenyang 110819, China; shenyanbai@mail.neu.edu.cn (Y.S.); zhaosikai@mail.neu.edu.cn (S.Z.); zhaoqiang@mail.neu.edu.cn (Q.Z.); zhoushijie@mail.neu.edu.cn (S.Z.)
[2] State Key Laboratory of Process Automation in Mining & Metallurgy, Beijing 100160, China
* Correspondence: hancong@mail.neu.edu.cn (C.H.); aoyuxin@gmail.com (Y.A.)

**Abstract:** Cerussite is an essential lead oxide mineral with increasing economic importance as lead sulfide resources deplete. This study utilizes density functional theory (DFT) to investigate the structural and electronic properties of the sulfurized cerussite (110) surface. The results show that when the cerussite crystal cleaves along the (110) plane, only the surface layer atoms undergo relaxation to reconstruct the surface, while the atoms located deeper have almost no impact on the reconstructed surface structure. The Pb atoms on the cerussite (110) surface react with the sulfurizing agent to form a PbS deposition layer with a structure similar to galena. This PbS deposition layer is tightly adsorbed onto the lead oxide layer through Pb-S bonds formed by S and subsurface lead oxide structure Pb atoms. The chemical reactivity of Pb atoms in the PbS layer on the sulfurized cerussite (110) surface is more potent than that of Pb atoms on the galena surface; additionally, the Pb atoms closer to the lead oxide layer exhibit slightly higher chemical reactivity than those farther away. This study provides insight into sulfurized cerussite surfaces' structure and properties at an atomic level and assists in explaining the floating behavior of cerussite.

**Keywords:** cerussite; sulfidation; surface property; DFT



**Citation:** Han, C.; Ao, Y.; Shen, Y.; Zhao, S.; Zhao, Q.; Zhou, S. Density Functional Theory Study on Structure and Properties of Sulfurized Cerussite (110) Surface. *Minerals* **2024**, *14*, 801. https://doi.org/10.3390/min14080801

Academic Editor: Jordi Ibanez-Insa

Received: 28 June 2024
Revised: 2 August 2024
Accepted: 5 August 2024
Published: 7 August 2024



## 1. Introduction

Lead is a metal of significant industrial importance, widely used in producing batteries, radiation shielding, and various alloy materials [1–3]. The primary raw materials for producing lead metal come from natural lead-bearing minerals. Lead-bearing minerals are mainly classified into sulfide lead minerals and oxide lead minerals [4]. Sulfide lead minerals, such as galena, have historically been the primary source of lead due to their abundance and ease of extraction. Industrially valuable minerals include galena (PbS), a sulfide mineral, cerussite ($PbCO_3$), and anglesite ($PbSO_4$), which are oxide minerals. Each type of mineral has unique characteristics and processing requirements that influence how lead is extracted and refined. Galena is the most common and has the highest utilization rate among lead-bearing minerals. It is typically found in hydrothermal veins and as a byproduct in the mining of other metals, such as zinc and silver [5]. However, with the depletion of easily separable sulfide lead mineral resources, the proportion of oxide lead minerals in producing lead metal raw materials is gradually increasing. This shift is because many high-grade sulfide deposits have been extensively mined, leading to the need for alternative sources [6–10].

Cerussite ($PbCO_3$) is an important oxide lead mineral commonly found in the oxidized zones of lead–zinc deposits [11]. With the decreasing availability of sulfide lead minerals resources, its economic importance has grown. Cerussite has a chemical composition of $PbCO_3$, with a theoretical lead content of 77.6%. It cleaves along (110), exhibits uneven or shell-like fracture surfaces, and has a hardness of 3.0~3.5 and a density of 6400.0~6600.0 kg/m$^3$ [12,13]. Its relatively high lead content makes it a valuable mineral

for lead extraction [14]. Cerussite effervesces in hydrochloric acid, a property that is useful in distinguishing it from sulfide lead minerals. Typically, cerussite forms when galena oxidizes to anglesite, which then interacts with carbonate-rich aqueous solutions. This process often occurs in the supergene zone, where surface weathering converts primary sulfide minerals into secondary oxide minerals. Cerussite is often found in the oxidized zones of lead–zinc sulfide deposits and is commonly utilized alongside primary lead minerals as an ore of lead [4].

Flotation is the primary method used to recover cerussite from ores. This process involves the separation of valuable minerals from the gangue based on differences in their hydrophobic properties. However, the natural floatability of cerussite is poor, and direct flotation using xanthate, a common flotation reagent, usually yields unsatisfactory results [15,16]. This is because cerussite's surface properties make it less amenable to commonly used xanthate collector adsorption; therefore, activating agents are commonly added during cerussite flotation to modify its surface properties, making it more amenable to adsorption by collectors. Sodium sulfide is the most widely used activating agent in cerussite flotation [17]. Its activation mechanism involves the dissociation of sodium sulfide in water into sodium ions and sulfide ions. These sulfide ions then react with lead ions on the cerussite surface, forming a lead sulfide (PbS) layer that imparts surface properties similar to those of galena, enhancing the adsorption of xanthate [16,18]. This transformation is crucial for improving the efficiency of the flotation process, as it allows for better separation of cerussite from the ore's low cost.

Extensive research has been conducted on the mechanism of sodium sulfide sulfidation of cerussite surfaces. Studies have elucidated the types of adsorption, adsorption sites, and electron transfer patterns among surface atoms before and after the adsorption of dissolved components of sodium sulfide on the cerussite surface. These insights enhance our understanding of the cerussite sulfidation process, revealing the complexities of surface chemistry and how they influence flotation efficiency [19–26]. However, since the sulfidation of cerussite occurs only within a few atomic layers on the mineral surface, the electronic structure of atoms within the lead sulfide layer formed by sulfidation is also influenced by atoms in the oxide lead layer in the bulk phase, resulting in the differences of a sulfurized cerussite surface from the surface properties of galena. Although current research has explained the mechanism of sulfide formation on the surface of cerussite, studies on the electronic properties of atoms in the sulfide-oxide binary heterostructure surface layer formed after the sulfidation of cerussite have not yet been systematically studied. This situation highlights the need for more detailed studies on the properties of sulfurized cerussite surfaces, which could provide insights into the processes of cerussite sulfurize flotation. Density functional theory (DFT) is a widely used method for studying the electronic structure of materials. It allows for the analysis of changes in the surface structure and electronic properties of sulfurized cerussite from a microscopic perspective [27–32]. In our study, we used DFT methods to simulate the surface structure and electronic properties of sulfurized cerussite. These results provide detailed insights into the atomic-level interactions and electron density redistribution within the sulfide–oxide binary heterostructure on the cerussite surface, deepening our understanding of the flotation behavior of sulfurized cerussite.

## 2. Computational Methods

### *2.1. Calculation Method and Main Parameters*

The DFT calculations were performed using the quantum mechanical program Cambridge Sequential Total Energy Package (CASTEP) module of the Materials Studio V6.1 (MS 6.1), produced by the BIOVIA company (San Diego, CA, USA). The initial cell model of cerussite was constructed based on the lattice constant determined through physical experiments, with a = 5.1832 Å, b = 8.4492 Å, c = 6.1475 Å, $\alpha = \beta = \gamma = 90^{\circ}$, and Pmcn space group [33]. The electronic structure of the mineral surface was calculated based on the optimized surface models, with the parameter settings being consistent with

those used during the geometric structure optimization. The valence electron configurations for the Pb, C, O, and S atoms involved in the calculations were $5d^{10}6s^26p^2$, $2s^22p^2$, $2s^22p^4$, and $3s^23p^4$, respectively. The exchange-correlation functional, the density of k-mesh in the Brillouin zone, and the energy cutoff for the plane wave basis set used in the calculations were determined based on the testing results. In the calculations, the norm-conserving pseudopotential was used to handle plane waves, and the Pulay Density mixing method was employed for electronic self-consistency, with a convergence criterion of $1.0 \times 10^{-6}$ eV/atom. For the optimization of the mineral crystal geometric structure and the calculation of properties, the convergence accuracy for the Energy, Max. force, Max. displacement, and Max stress were set to $2 \times 10^{-5}$ eV/atom, 0.05 eV/Å, 0.002 Å, and 0.1 GPa, respectively.

### *2.2. Construction of Surface Model*

The surface model of cerussite was constructed by cleaving the initial cell model along the (110) plane. The thickness of the cleaved slab model is the thickness of three $PbCO_3$ units perpendicular to the cerussite (110) plane. To prevent interactions between the adjacent (110) plane due to periodic boundary conditions during the simulation, we added a 20 Å vacuum layer on the cleaved slab model in the C-axis direction. Through un-constraining the coordinates of atoms within a certain depth range from the surface and constraining the coordinates of the other bottom atoms of the initial slab model, the number of surface atoms involved in the reconstruction is altered. Through comparing the surface energies ($E_{surface}$), the cerussite (110) slab model was determined to be used for subsequent simulations. Based on this, the sulfide–oxide binary heterostructure model for the sulfurized cerussite surface was constructed. The surface energy calculation formula for the mineral surface structure model is shown in Equation (1), where $N_{slab}$ and $N_{bulk}$ are the numbers of atoms contained in the slab and the bulk models, respectively; $E_{slab}$ and $E_{bulk}$ are the total energy of the slab and the bulk models, respectively; $A$ is the surface area of the slab model; and the number 2 denotes the number of new surfaces formed when cutting the bulk model to build the slab model [34]:

$$E_{surface} = \frac{E_{slab} - \left(\frac{N_{slab}}{N_{bulk}}\right) \times E_{bulk}}{2A} \quad (1)$$

## 3. Results and Discussion

### *3.1. Determination of Primarily Parameters*

The lattice constants of cerussite using the Generalized Gradient Approximation (GGA) and its associated functionals were calculated under the condition that the cutoff energy was 700 eV and the Brillouin zone k-mesh density was $2 \times 1 \times 2$. The results are shown in Table 1, where the "Lattice Constant Difference" represents the sum of the deviations in the calculated values of lattice constant a, b, and c from the experimental values.

As shown in Table 1, the calculated lattice constant of cerussite using the GGA and its associated functionals exhibit some discrepancies compared to the experimentally measured lattice constant. Among these, the lattice constant calculated using the RPBE functional show the most significant deviation from the experimental values, while those calculated using the PW91 functional show the slightest deviation. The lattice constant calculated using the PBE, WC, and PBESOL functionals exhibit similar deviations from the experimental values. Therefore, the PW91 functional was selected for subsequent calculations to ensure accuracy.

The influence of the Brillouin zone k-mesh density on the lattice constant of cerussite was investigated under the condition of using the GGA+PW91 functional and a cutoff energy of 700 eV, and the results are shown in Table 2.

**Table 1.** Experimental and calculated values of lattice constant of cerussite using different exchange-correlation functionals.

| | Functionals | Lattice Constant | | | Difference/% |
|---|---|---|---|---|---|
| | | a/Å | b/Å | c/Å | |
| Experimental | | 5.1832 | 8.4492 | 6.1475 | |
| Simulation | GGA-PBE [35] | 5.2140 | 8.4673 | 6.2855 | 3.215 |
| | GGA-RPBE [36] | 5.3763 | 8.5006 | 6.9485 | 16.771 |
| | GGA-PW91 [37] | 5.2052 | 8.4496 | 6.2499 | 2.674 |
| | GGA-WC [38] | 5.1232 | 8.4041 | 6.0907 | 3.201 |
| | GGA-PBESOL [39] | 5.1258 | 8.4029 | 6.0904 | 3.169 |

**Table 2.** Experimental and calculated lattice constant of cerussite using different k-mesh densities.

| | K-Mesh Density | Lattice Constant | | | Difference/% |
|---|---|---|---|---|---|
| | | a/Å | b/Å | c/Å | |
| Experimental | | 5.1832 | 8.4492 | 6.1475 | |
| Simulation | $1 \times 1 \times 1$ | 5.3117 | 10.8946 | 4.7890 | 52.759 |
| | $2 \times 1 \times 2$ | 5.2052 | 8.4496 | 6.2499 | 2.674 |
| | $3 \times 2 \times 2$ | 5.2106 | 8.4794 | 6.2434 | 2.320 |
| | $4 \times 3 \times 2$ | 5.2104 | 8.4815 | 6.2416 | 2.264 |
| | $5 \times 3 \times 2$ | 5.2091 | 8.4823 | 6.2398 | 2.200 |

Table 2 shows that when the Brillouin zone k-mesh density is $1 \times 1 \times 1$, the deviation between the calculated lattice constant of cerussite and the experimental values is the largest, at 52.759%. When the Brillouin zone k-mesh density is increased beyond $2 \times 1 \times 2$, the deviation between the calculated and experimental lattice constant gradually decreases, but the reduction is marginal, within 0.4%. Since increasing the Brillouin zone k-mesh density will significantly increase the computational load, the k-point density $2 \times 1 \times 2$ was selected for subsequent calculations.

The influence of the cutoff energy on lattice constant of cerussite was investigated under the condition of using GGA+PW91 functional and the Brillouin zone k-mesh density is $2 \times 1 \times 2$, and the results are shown in Table 3.

**Table 3.** Experimental and calculated lattice constant of cerussite using different cutoff energy values.

| | Cutoff Energy/eV | Lattice Constant | | | Difference/% |
|---|---|---|---|---|---|
| | | a/Å | b/Å | c/Å | |
| Experimental | | 5.1832 | 8.4492 | 6.1475 | |
| Simulation | 600 | 5.2385 | 8.4646 | 6.3399 | 4.605 |
| | 650 | 5.2148 | 8.4696 | 6.2919 | 3.306 |
| | 680 | 5.2235 | 8.4383 | 6.3030 | 4.023 |
| | 700 | 5.2052 | 8.4496 | 6.2499 | 2.674 |
| | 720 | 5.2019 | 8.4424 | 6.2513 | 2.717 |

As the results show in Table 3, the deviation between the calculated lattice constant of cerussite and the experimental values gradually decreases with an increase in plane wave cutoff energy. When the cutoff energy is increased to 700 eV, the deviation between the calculated and experimental lattice constant is less than 0.05%. Considering that increasing the cutoff energy also increases the computational load and that an excessively high cutoff energy does not further improve the calculation accuracy, the cutoff energy of 700 eV was selected for subsequent calculations.

### *3.2. Geometry and Electronic Structure of Cerussite (110) Plane*

The force field environment experienced by atoms at the surface of the mineral differs from that of the inner atoms of the mineral. When the mineral crystal cleaves along a particular plane to form a new surface, the net external force acting on the surface atoms is no longer zero. These surface atoms will relax under the influence of forces from the interior atoms to form a new surface structure that reduces the surface energy and locates into a new equilibrium state. The surface atoms mentioned here are the atoms in one or several layers close to the newly formed surface. After the formation of the new surface, these atoms undergo relaxation due to changes in the resultant force they experience. They move into new equilibrium positions, resulting in the reconstruction of the new surface structure and contribution to the surface energy. The farther these surface atoms are from the surface, that is, the greater their depth, the smaller the resultant force from other atoms, making relaxation less likely. When the depth increases a certain value, the resultant force experienced by atoms at this depth is similar to the atoms at the deeper location, and they no longer undergo relaxation. In other words, atoms located at this depth or deeper no longer participate in surface reconstruction. To determine the depth of the atoms that participate in surface reconstruction, the surface energy of the cerussite (110) plane after reconstruction was calculated. The initial model before geometry optimization, the range of unconstrained atoms during geometry optimization, the optimized model with atomic coordinates unconstrained within a depth of 8.864 from the surface, and the Mulliken charge of the surface atoms (the first $PbCO_3$ unit) are shown in Figure 1, and the surface energy calculation results are presented in Figure 2.

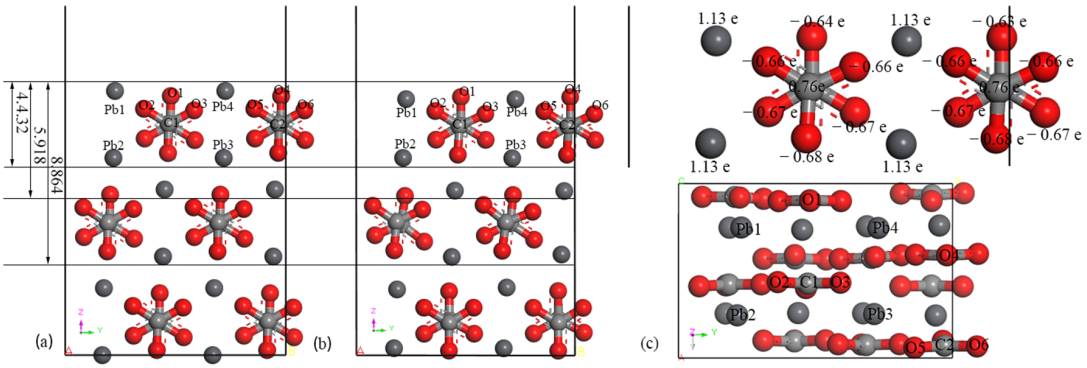


**Figure 1.** Structure of cerussite (110) plane (**a**): front view of initial model before geometry optimization and the range of unconstrained atoms; (**b**,**c**): front and top view of the optimized model with atomic coordinates unconstrained within a depth of 8.864 Å from the surface.

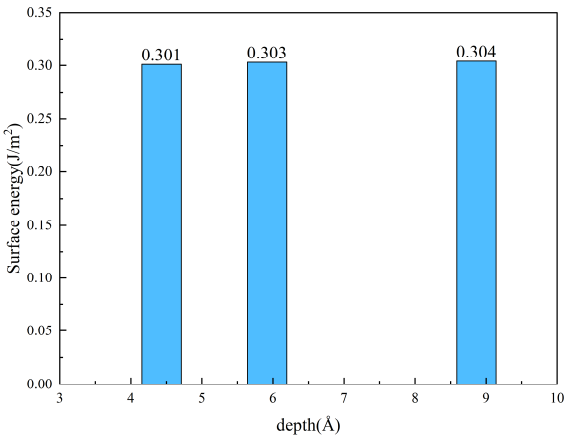


**Figure 2.** Surface energy of cerussite (110) plane after atomic relaxation when atoms in different depth ranges are unconstrained.

It can be observed from Figures 1 and 2 that the surface energy of the reconstructed cerussite (110) plane does not exhibit significant changes with increasing depth of the unconstrained atoms, which is about 0.3 $J/m^2$ with a variation not exceeding 0.002 $J/m^2$. The Pb atoms located in the surface layer relax toward the interior of the crystal perpendicular to the surface, while the C and O atoms that constitute the $CO_3^{2-}$ do not show significant displacement; additionally, the positions of Pb, O, and C atoms in the deeper layers also do not exhibit noticeable changes, all of which indicate that after the cerussite crystal cleaves along the (110) plane, only the atoms located near the surface undergo relaxation and surface reconstruction, and the atoms in the deeper layers perpendicular to the surface have little impact on the reconstructed surface structure. Therefore, it can be inferred that when the cerussite (110) plane is sulfurized, only the Pb atoms in the shallow surface layers react with the sulfurizing agent.

Figure 3 is the total and partial density of states (TDOS and PDOS) of the unconstrained atoms located within the depth of 8.864 Å after the surface reconstruction of the cerussite (110) plane. This shows that the valence electrons of Pb, C, and O atoms contribute to the TDOS, and the conduction band is mainly contributed to by the 6p orbitals of Pb atoms, 2s orbitals and 2p orbitals of C atoms, and 2s orbitals and 2p orbitals of O atoms. The upper valence band (−10.0~0.0 eV) is mainly contributed to by 2s and 2p orbitals of C atom, 2s and 2p orbitals of O atom, and 6s orbitals of Pb atom. The lower valence band (−30.0~−10.0 eV) is mainly contributed to by the 5d orbital of Pb atom, the 2s orbital and 2p orbital of C atom, and the 2s orbital of O atom. In the upper and lower valence bands, the s and p orbitals of C and O atoms show obvious coincidence, which indicates that there is a strong bonding between them. The 5d orbital of the Pb atoms shows sharp peaks and does not overlap with the electronic orbitals of other atoms, indicating that the electrons in it have a high effective mass, a high localization degree, and limited orbital extension. This suggests that these electrons are less likely to participate in bonding during chemical reactions. The energy bands of the Pb atom's 6s and 6p orbitals cross the Fermi level (0.0 eV), indicating that the electrons in the Pb atom's 6s and 6p orbitals can transfer from the valence band to the conduction band, which suggests that the electrons in Pb atom's 6s and 6p orbitals could participate in the chemical reaction, meaning that in the flotation process, the Pb atoms on the surface of cerussite can serve as sites for the chemical adsorption of flotation reagents.

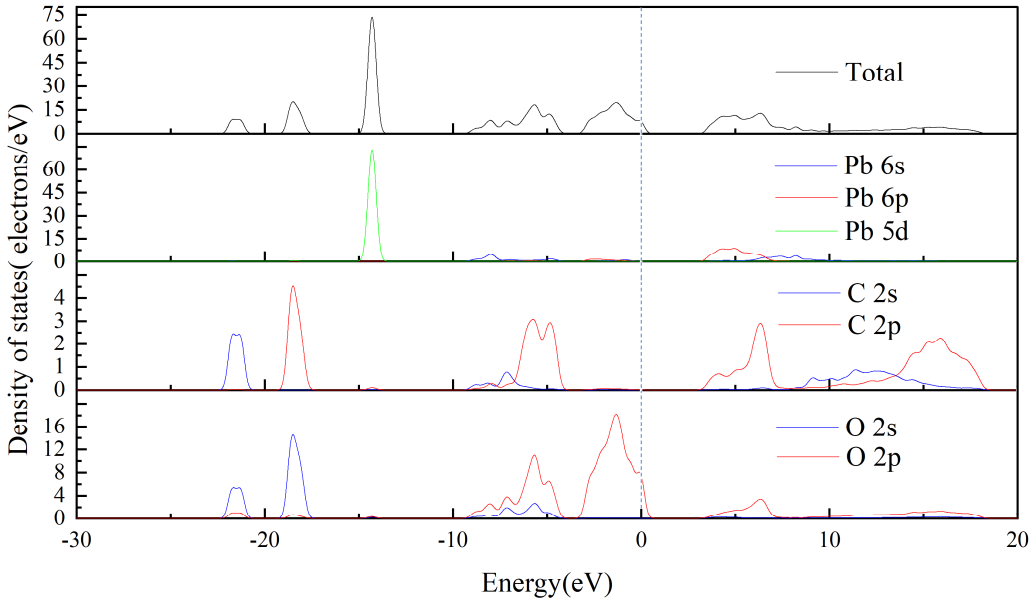


**Figure 3.** Total density of state and partial density of state of atoms of cerussite (110) plane.

### *3.3. Geometry and Electronic Structure of Sulfurized Cerussite (110) Plane*

While cerussite is sulfurized, a series of chemical reactions occur on its surface, generally divided into three steps. The first step is the sulfide components adsorbed onto the surface of cerussite, which commonly are S and HS dissociated from sodium sulfide. The second step is chemical reactions between the adsorbed sulfide ions and the cerussite surface, forming PbS. The final step consists of depositing the formed PbS on the surface of cerussite, gradually forming a layer of PbS coverage [10,19]. The study results of the surface energy of the cerussite (110) plane shown in Figure 2 reveal that only the shallow layers (1 $PbCO_3$ unit) of atoms near the surface undergo relaxation; meanwhile, Pb atoms that react with the sulfuring agent are predominantly located in the outermost layers of the surface. Therefore, in studying the surface structure of cerussite after sulfidation, only the deposition of PbS generated from the reaction of surface-layer (1 $PbCO_3$ unit) lead atoms with the sulfuring agent on the cerussite (110) plane is considered. To minimize the impact of structural changes on the research results and based on the study results shown in Figure 2, we selected the optimized slab model of the cerussite (110) plane of which atoms within 8.864 Å from the surface are unconstrained. Then, we constructed the sulfurized cerussite (110) plane slab model by assuming that its top $PbCO_3$ unit layer completely dissolves, reacts with the sulfuring agent, and then redeposits as a PbS layer on the remaining lead oxide structure. Subsequently, geometric optimization and electronic structure calculations were performed on this model. The optimized surface configuration of the sulfurized cerussite (110) plane and the Mulliken charge of the surface atoms (S1~S4, Pb1~Pb4) are shown in Figure 4, and the electronic structure of the Pbs deposition layer (S1~S4, Pb1~Pb4) is shown in Figure 5.

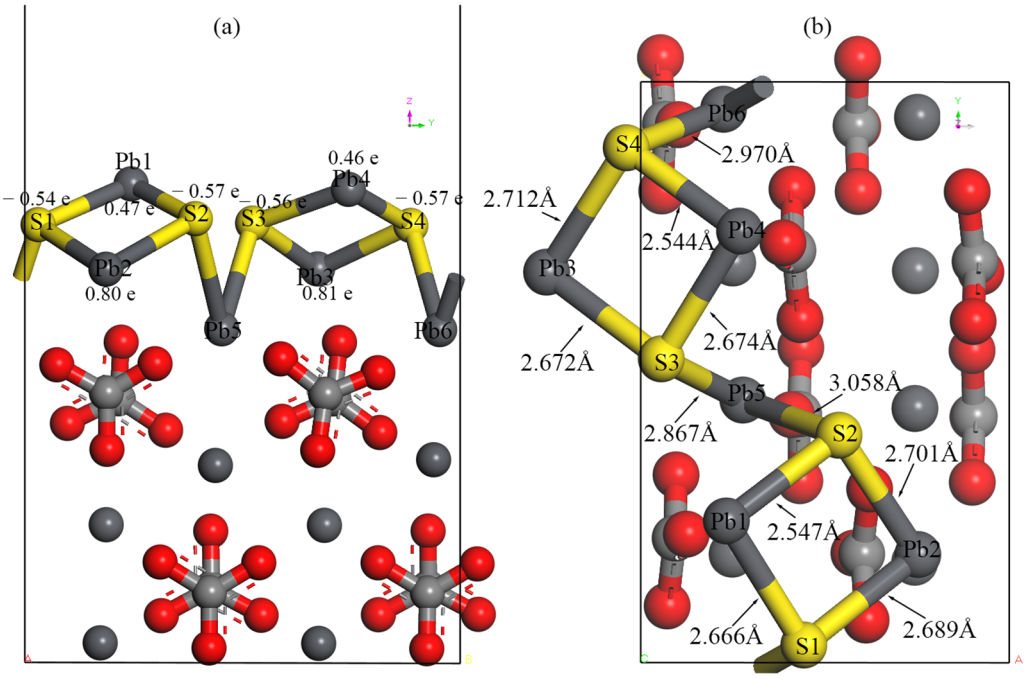


**Figure 4.** The optimized surface configuration of the sulfurized cerussite (110) plane ((**a**): front view; (**b**): top view)).

Figure 4 shows that the sulfur-containing ion components dissociated from the sulfide reagent react with Pb ions to form PbS, which deposits on the cerussite (110) plane, forming a structure similar to galena. It then, through the S-Pb bond, binds with the Pb ions inside the cerussite lattice and tightly adsorbs on the surface of the cerussite to form a heterostructure of sulfide–oxide. The S-Pb bond lengths of the deposited PbS located on the sulfurized cerussite (110) plane range between 2.544 Å and 2.712 Å, shorter than the S-Pb bond length of 2.966 Å typically found in galena [40]. The S-Pb bond lengths for

bonds (S4-Pb4, S3-Pb4, S2-P1, and S1-Pb1) located farther from the underlying cerussite oxide structure are relatively shorter, whereas those for bonds (S3-Pb3, S4-Pb3, S2-Pb2, and S1-Pb2) closer to the underlying cerussite oxide structure are relatively longer. The bond lengths of the S-Pb bonds (S2-Pb5, S3-Pb5, and S4-Pb6) formed between sulfur atoms in the PbS deposition layer and Pb atoms in the cerussite lattice range from 2.867 Å to 3.058 Å, which are longer than the bond lengths of S-Pb bonds in the PbS deposition layer and closer to the bond lengths of S-Pb bonds in galena.

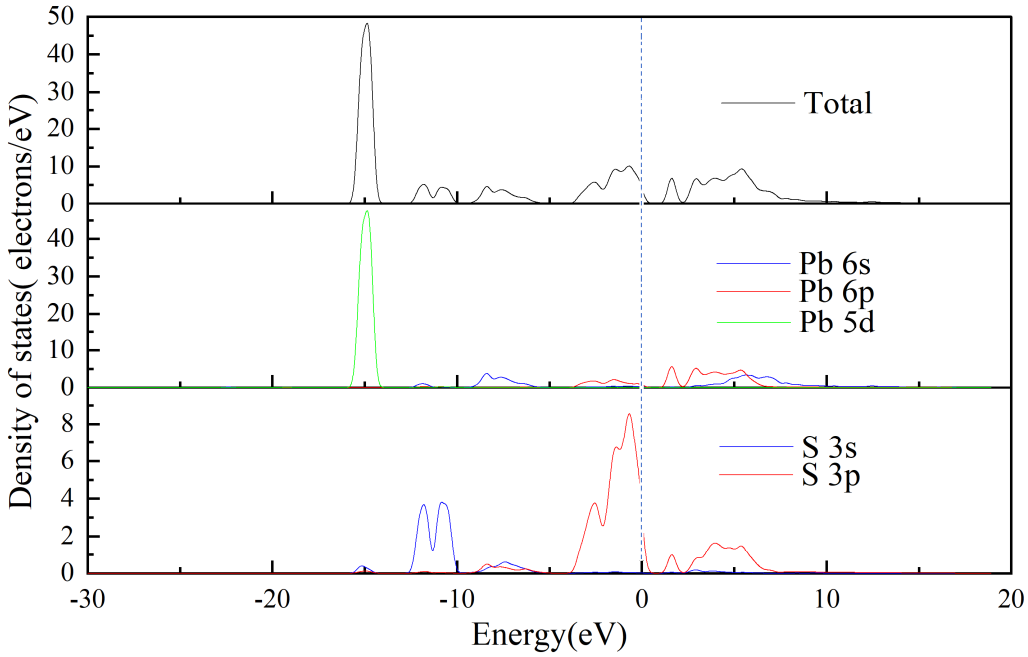


**Figure 5.** TDOS and PDOS of atoms' electrons in PbS layer of sulfurized cerussite (110) plane.

As revealed by Figure 5, within the upper and lower valence bands (−20.0~−0.0 eV) of the PbS deposit layer, the s and p orbitals of Pb and S atoms exhibit notable overlaps, which indicates the presence of strong bonding between these two types of atoms. The 5d orbital of Pb atoms is a sharp peak with strong localization, resulting in the electrons having difficulty participating in forming chemical bonds. The 6s and 6p orbitals of Pb atoms cross the Fermi level, indicating that Pb atoms can serve as chemical adsorption sites for flotation reagents. Compared to the PDOS (Figure 3) of Pb atoms of the cerussite (110) plane, the density of states of the Pb atoms on the sulfurized cerussite (110) plane increases near the Fermi level, meaning that it shows more chemical reactivity than the former.

To further investigate the impact of the sulfide–oxide binary heterostructure on the electronic structure of Pb atoms on the sulfurized cerussite (110) plane, the PDOSs of the valence electrons of Pb1 to Pb4 atoms were analyzed. As shown in Figure 6, the PDOSs of the valence electrons of Pb1 and Pb4 atoms, which are relatively distant from the underlaying lead oxide structure, are similar. Likewise, the PDOSs for Pb2 and Pb3 atoms, which are relatively close to the underlying lead oxide structure, are similar. The density of states of 6s and 6p orbital electrons of Pb1 and Pb4 atoms near the Fermi level is higher than those of Pb2 and Pb3 atoms. The high density of states provides more possible electron exchange paths; therefore, Pb2 and Pb3 atoms are more inclined than Pb1 and Pb4 atoms to transfer electrons and form chemical bonds with the polar groups of flotation reagents such as xanthate.

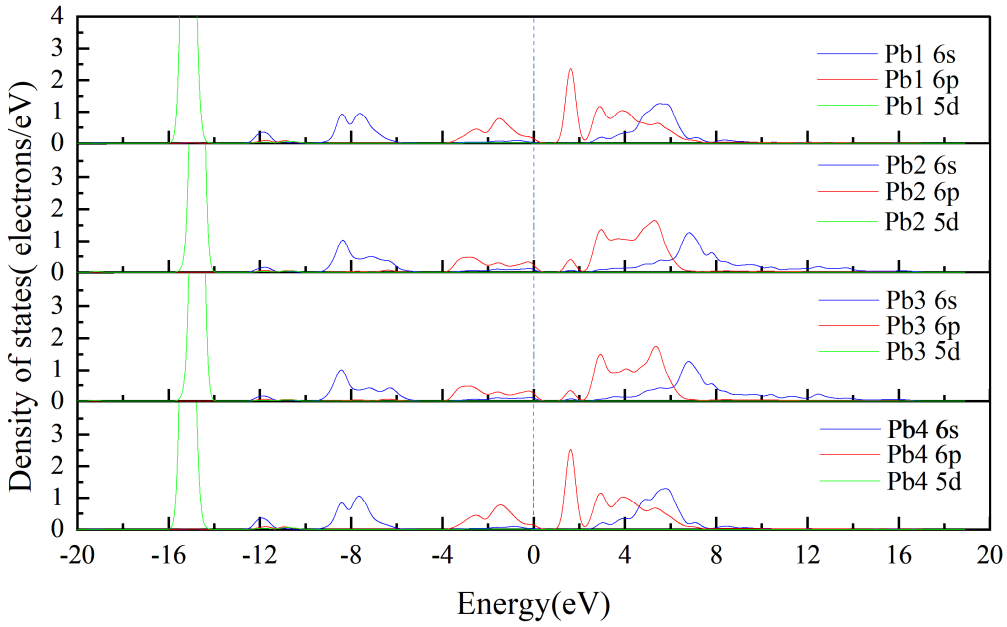


**Figure 6.** PDOSs of valence electrons of Pb atoms on surface of sulfurized cerussite (110) plane.

## 4. Conclusions

This study demonstrates the surface structure and properties of sulfurized cerussite surfaces at the atomic level, further deepening and enriching the understanding of the surface properties of sulfurized cerussite. From the above results, the following primary conclusions are obtained:

(1) Upon the cleavage of the cerussite crystal along the (110) plane, only the shallow-layer atoms near the newly formed surface undergo relaxation to reconstruct the surface, resulting in a surface energy of approximately 0.3 $J/m^2$.

(2) Only the surface-layer Pb atoms of the cerussite (110) plane react with the sulfuring agent to form PbS, which forms a structure similar to galena on the cerussite surface. The Pb-S bond length in the newly formed PbS layer is shorter than in galena, and the Pb-S bonds formed between S atoms in the newly formed PbS layer and Pb atoms in the cerussite lattice have longer bond lengths, approaching that observed in galena.

(3) The density of states of the Pb atoms on the sulfurized cerussite (110) surface increases near the Fermi level compared with that of the Pb atoms of the cerussite (110) plane, resulting in the former being more easily adsorbed by a flotation reagent such as xanthate.

(4) The Pb atoms of the sulfide layer that are relatively distant from the lead oxide structure have their 6s and 6p orbital electrons occupying energy levels closer to the Fermi level than those of Pb atoms that are in closer proximity to the lead oxide structure, indicating that these orbital electrons show stronger localization, which implies that electron transfer between Pb and the polar groups of flotation reagents occur more easily.

**Author Contributions:** Conceptualization, C.H. and Y.A.; methodology, C.H., Y.S. and Q.Z.; software, S.Z. (Sikai Zhao) and S.Z. (Shijie Zhou); validation, Y.A., C.H. and S.Z. (Sikai Zhao); formal analysis, C.H. and Y.S.; investigation, C.H. and Y.A.; resources, C.H.; writing—original draft preparation, C.H.; writing—review and editing, C.H. and Y.S.; visualization, Q.Z.; supervision, C.H. and Y.S.; project administration, C.H.; funding acquisition, C.H. All authors have read and agreed to the published version of the manuscript.

**Funding:** This research was funded by the National Natural Science Foundation of China under grant number 52374261, and the Open Foundation of State Key Laboratory of Process Automation in Mining & Metallurgy (BGRIMM-KZSKL-2021-12).

**Data Availability Statement:** The original contributions presented in the study are included in the article, further inquiries can be directed to the corresponding author/s.

**Conflicts of Interest:** The authors declare no conflict of interest.

## References


1. Geoffrey, J. May, Alistair Davidson and Boris Monahov, Lead batteries for utility energy storage: A review. *J. Energy Storage* **2018**, *15*, 145–157. [CrossRef]
2. AbuAlRoos, N.J.; Amin, N.A.B.; Zainon, R. Conventional and new lead-free radiation shielding materials for radiation protection in nuclear medicine: A review. *Radiat. Phys. Chem.* **2019**, *165*, 108439. [CrossRef]
3. Chen, L.; Li, T.; Zhang, J.; Wang, Y.; Kong, L.; Xu, B.; Yang, B.; Wu, M. Modeling and measurement of vapor-liquid equilibrium of In–Pb and In–Pb–Sn alloy systems in vacuum distillation. *Vacuum* **2023**, *207*, 111556. [CrossRef]
4. Chen, Y.; Sun, Y.; Han, Y. Efficient flotation separation of lead–zinc oxide ores using mineral sulfidation reconstruction technology: A review. *Green Smart Min. Eng.* **2024**, *1*, 175–189. [CrossRef]
5. Westner, K.J.; Vaxevanopoulos, M.; Blichert-Toft, J.; Davis, G.; Albarède, F. Isotope and trace element compositions of silver-bearing ores in the Balkans as possible metal sources in antiquity. *J. Archaeol. Sci.* **2023**, *155*, 105791. [CrossRef]
6. Li, S.; Shi, Q.; Li, B.; Yu, Y. Separation of cerussite and calcite by flotation using tert-butylbenzylhydroxamic acid collector and insights to its adsorption mechanism. *J. Mol. Liq.* **2024**, *407*, 125271. [CrossRef]
7. Li, Y.; Wang, J.-K.; Wei, C.; Liu, C.-X.; Jiang, J.-B.; Wang, F. Sulfidation roasting of low grade lead–zinc oxide ore with elemental sulfur. *Miner. Eng.* **2010**, *23*, 563–566. [CrossRef]
8. Moradi, S.; Monhemius, A.J. Mixed sulphide–oxide lead and zinc ores: Problems and solutions. *Miner. Eng.* **2011**, *24*, 1062–1076. [CrossRef]
9. Önal, G.; Bulut, G.; Gül, A.; Kangal, O.; Perek, K.T.; Arslan, F. Flotation of Aladağ oxide lead–zinc ores. *Miner. Eng.* **2005**, *18*, 279–282. [CrossRef]
10. Wei, Q.; Dong, L.; Qin, W.; Jiao, F.; Qi, Z.; Feng, C.; Sun, D.; Wang, L.; Xiao, S. Efficient flotation recovery of lead and zinc from refractory lead-zinc ores under low alkaline conditions. *Geochemistry* **2021**, *81*, 125769. [CrossRef]
11. Sotillo, F.J.; Herrera-Urbina, R.; Fuerstenau, D.W. Amyl xanthate uptake by natural and sulfide-treated cerussite and galena. *Int. J. Miner. Process.* **1998**, *55*, 113–128. [CrossRef]
12. Sánchez-Navas, A.; López-Cruz, O.; Velilla, N.; Vidal, I. Crystal growth of lead carbonates: Influence of the medium and relationship between structure and habit. *J. Cryst. Growth* **2013**, *376*, 1–10. [CrossRef]
13. Ye, Y.; Smyth, J.R.; Boni, P. Crystal structure and thermal expansion of aragonite-group carbonates by single-crystal X-ray diffraction. *Am. Mineral.* **2012**, *97*, 707–712. [CrossRef]
14. Elizondo-Álvarez, M.A.; Uribe-Salas, A.; Nava-Alonso, F. Flotation studies of galena (PbS), cerussite ($PbCO_3$) and anglesite ($PbSO_4$) with hydroxamic acids as collectors. *Miner. Eng.* **2020**, *155*, 106456. [CrossRef]
15. Zheng, Y.-X.; Bao, L.-Y.; Lv, J.-F.; Pang, J.; Hu, P.-J.; Huang, Y.-S. Flotation response of cerussite after hydrothermal treatment with sulfur and the sulfidation mechanism. *J. Mater. Res. Technol.* **2021**, *15*, 2933–2942. [CrossRef]
16. Herrera-Urbina, R.; Sotillo, F.J.; Fuerstenau, D.W. Effect of sodium sulfide additions on the pulp potential and amyl xanthate flotation of cerussite and galena. *Int. J. Miner. Process.* **1999**, *55*, 157–170. [CrossRef]
17. Li, C.-X.; Wei, C.; Deng, Z.-G.; Li, X.-B.; Li, M.-T.; Xu, H.-S. Hydrothermal Sulfidation and Flotation of Oxidized Zinc-Lead Ore. *Metall. Mater. Trans. B* **2014**, *45*, 833–838. [CrossRef]
18. Feng, Q.; Wen, S.; Deng, J.; Zhao, W. Combined DFT and XPS investigation of enhanced adsorption of sulfide species onto cerussite by surface modification with chloride. *Appl. Surf. Sci.* **2017**, *425*, 8–15. [CrossRef]
19. Chen, J.; Lan, L.; Chen, Y. Computational simulation of adsorption and thermodynamic study of xanthate, dithiophosphate and dithiocarbamate on galena and pyrite surfaces. *Miner. Eng.* **2013**, *46–47*, 136–143. [CrossRef]
20. Karamoozian, M.; Karamoozian, M. Proposing a seven-parameter kinetics model for predicting cerussite flotation recovery. *Int. J. Min. Geo-Eng.* **2020**, *54*, 1–12. [CrossRef]
21. Li, J.; Liu, S.; Liu, D.; Liu, R.; Liu, Z.; Jia, X.; Chang, T. Sulfidization mechanism in the flotation of cerussite: A heterogeneous solid-liquid reaction that yields $PbCO_3$/PbS core-shell particles. *Miner. Eng.* **2020**, *153*, 106400. [CrossRef]
22. Liu, C.; Zhang, W.; Song, S.; Li, H.; Jiao, X. A novel insight of the effect of sodium chloride on the sulfidization flotation of cerussite. *Powder Technol.* **2019**, *344*, 103–107. [CrossRef]
23. Moimane, T.; Peng, Y. Sulphidisation of oxides and oxidised sulphides and adsorption of thiol collectors on the sulphidised products-a critical review. *Adv. Colloid Interface Sci.* **2020**, *305*, 102697. [CrossRef] [PubMed]
24. Fuerstenau, M.C.; Olivas, S.A.; Herrera-Urbina, R.; Han, K.N. The surface characteristics and flotation behavior of anglesite and cerussite. *Int. J. Miner. Process.* **1987**, *20*, 73–85. [CrossRef]
25. Zhang, Q.; Wen, S.; Zhang, S.; Feng, Q. Surface chemistry of dissolved species of cerussite and calcite and its effect on flotation performance. *Colloids Surf. A Physicochem. Eng. Asp.* **2022**, *646*, 128945. [CrossRef]
26. Tang, X.; Chen, J.; Chen, Y. A density functional based tight binding (DFTB+) study on the sulfidization-xanthate flotation mechanism of cerussite. *Appl. Surf. Sci.* **2023**, *612*, 155677. [CrossRef]

27. Richard, D.; Rendtorff, N.M. Kaolin group minerals under pressure: The study of their structural and electronic properties by DFT methods. *Appl. Clay Sci.* **2022**, *219*, 106444. [CrossRef]
28. Cui, W.; Chen, J. Insight into mineral flotation fundamentals through the DFT method. *Int. J. Min. Sci. Technol.* **2021**, *31*, 983–994. [CrossRef]
29. Sarvaramini, A.; Larachi, F.; Hart, B. Collector attachment to lead-activated sphalerite—Experiments and DFT study on pH and solvent effects. *Appl. Surf. Sci.* **2016**, *367*, 459–472. [CrossRef]
30. Mangwejane, S.S.; Mkhonto, P.P.; Ngoepe, P.E. Comparison of adsorption capacity of water and hydroxide with collector reagents on geversite ($PtSb_2$) mineral surface: A DFT-D insights. *Comput. Mater. Sci.* **2023**, *224*, 112174. [CrossRef]
31. Zhang, X.; Fang, J.; Feng, Y.; Zhang, J.; Guo, R.; Chen, J. The mechanism of water decomposition on surface of aluminum and gallium alloy during the hydrogen production process: A DFT study. *Int. J. Hydrogen Energy* **2024**, *66*, 354–361. [CrossRef]
32. Zhao, C.; Zhou, X.; Chen, J. Ethyl xanthate adsorption on different surfaces of jamesonite: A DFT study. *Appl. Surf. Sci.* **2024**, *663*, 160135. [CrossRef]
33. Antao, S.M.; Hassan, I. The Orthorhombic Structure of $CaCO_3$, $SrCO_3$, $PbCO_3$ AND $BaCO_3$: Linear Structural Trends. *Can. Mineral.* **2009**, *47*, 1245–1255. [CrossRef]
34. Han, C.; Li, T.; Zhang, W.; Zhang, H.; Zhao, S.; Ao, Y.; Wei, D.; Shen, Y. Density Functional Theory Study on the Surface Properties and Floatability of Hemimorphite and Smithsonite. *Minerals* **2018**, *8*, 542. [CrossRef]
35. Perdew, J.P.; Burke, K.; Ernzerhof, M. Generalized Gradient Approximation Made Simple. *Phys. Rev. Lett.* **1996**, *77*, 3865–3868. [CrossRef] [PubMed]
36. Hammer, B.; Hansen, L.B.; Norskov, J.K. Improved adsorption energetics within density-functional theory using revised Perdew-Burke-Ernzerhof functionals. *Phys. Rev. B* **1999**, *59*, 7413. [CrossRef]
37. Perdew, J.P.; Chevary, J.A.; Vosko, S.H.; Jackson; Jackson, K.A.; Pederson, M.R.; Singh, D.J.; Fiolhais, C. Atoms, molecules, solids, and surfaces: Applications of the generalized gradient approximation for exchange and correlation. *Phys. Rev. B* **1993**, *46*, 6671. [CrossRef] [PubMed]
38. Wu, Z.; Cohen, R.E. More accurate generalized gradient approximation for solids. *Phys. Rev. B* **2006**, *73*, 235116. [CrossRef]
39. Perdew, J.P.; Ruzsinszky, A.; Csonka, G.I.; Vydrov, O.A.; Scuseria, G.E.; Constantin, L.A.; Zhou, X.; Burke, K. Restoring the Density-Gradient Expansion for Exchange in Solids and Surfaces. *Phys. Rev. Lett.* **2008**, *100*, 136406. [CrossRef]
40. Kang, J.; An, Y.; Xue, J.; Ma, X.; Li, J.; Chen, F.; Wang, S.; Wan, H.; Zhang, C.; Bu, X. Density Functional Theory Study of the Electronic Structures of Galena. *Processes* **2023**, *11*, 619. [CrossRef]